

Dust coagulation in infalling protostellar envelopes

I. Compact grains

Gerhard Suttner^{1,2}, Harold W. Yorke^{2,1}

¹*Astronomisches Institut der Universität Würzburg,
Am Hubland, 97074 Würzburg, Germany*

²*Jet Propulsion Laboratory, California Institute of Technology, MS 169-506,
4800 Oak Grove Drive, Pasadena, CA 91109, USA*

and

Doug N.C. Lin

UCO/Lick Observatory, UC Santa Cruz, Santa Cruz, CA 95060, USA

ABSTRACT

Dust plays a key role in the optical, thermodynamic and gas dynamical behavior of collapsing molecular cores. Because of relative velocities of the individual dust grains, coagulation and shattering can modify the grain size distribution and — due to corresponding changes in the medium's opacity — significantly influence the evolution during early phases of star formation. In order to study relevant time scales and possible consequences for intermediate-mass stars, we examine the dust evolution in spherical protostellar envelopes which evolve from cloud clumps of masses $3 M_{\odot}$, $5 M_{\odot}$ and $10 M_{\odot}$. At first the collapse proceeds in the well known non homologous manner until a central hydrostatic core is formed. During the non steady-state accretion the accretion luminosity of the central core reaches high values ($\approx 10^4 L_{\odot}$). Thus, differential radiative acceleration provides an important contribution to the relative velocities of the grains. In turn, the mass accretion rate, which determines the central core's accretion luminosity (and ultimately the final mass of the central object) depends strongly on the opacity distribution in the enshrouding envelope. We find that coagulation and shattering can lead to significant modifications of the dust size distribution and the opacity during early collapse phases. The visible and ultraviolet extinction is most strongly affected.

Subject headings: hydrodynamics – radiative transfer – circumstellar matter – stars: formation – dust, extinction

1. Introduction

Dust in star-forming regions is the principal source of extinction, preventing direct observation of dense molecular cloud cores at optical or near infrared wavelengths. Other contributors to the opacity, such as molecules or atoms can be neglected in this temperature and density regime (e.g., Yorke & Henning 1994). For high-mass stars the dust has generally been held responsible for limiting the final mass (e.g., Kahn 1974; Yorke & Krügel 1977; Wolfire & Cassinelli 1987). The formation and early evolution of stars of intermediate and low mass can be significantly influenced by the amount and types of dust present.

The dust opacity depends on the size distribution of the grains and their physical structure. For the diffuse interstellar medium, Mathis et al. (1977, hereafter MRN) derived a power law distribution as a function of grain radius with an exponent of about -3.3 to -3.6 (MRN distribution) by fitting observations of the interstellar extinction over the wavelength range $0.11 \mu\text{m}$ to $1 \mu\text{m}$. The sizes of the constituent grains were found to range from about 1 nm to $1 \mu\text{m}$, depending on the grain material. Observations (Vrba et al. 1993) and theoretical modeling of dense molecular clouds (Fischer et al. 1994), however, indicate larger upper grain sizes, implying that the grain size distribution has been modified in this environment.

Coagulation has long been considered the mechanism which produces large grains in star-forming regions and accretion disks (e.g., Weidenschilling 1980; Nakagawa et al. 1981; Mizuno et al. 1988, Schmitt et al. 1997). The prerequisite for coagulation is a relative velocity between the different dust grains. In dense cloud clumps Brownian motion and turbulence have been suggested as the most important processes (Ossenkopf 1993; Weidenschilling & Ruzmaikina 1994). These studies find characteristic coagulation time scales ranging from 10^5 up to 10^7 years. In particular, Weidenschilling & Ruzmaikina (1994) investigated the case of a collapsing cloud core. They found that the turbulence model assumed significantly influenced the results of the coagulation process. Strong turbulence, i.e., the eddy scale is proportional to the radius of the collapsing cloud, leads to a net destruction of large grains. Weak turbulence, i.e., the eddy scale varies slowly with the cloud radius, conserves the large grains but stalls coagulation due to strongly correlated particle speeds.

Differential radiative acceleration also leads to significant relative velocities between the grains, especially when a luminous protostellar radiation source is embedded in the cloud clump. However, coagulation is not the only process which modifies the size distribution. When the velocity between two grains becomes sufficiently high, coagulation ceases (Chokshi et al. 1993), then cratering starts, and finally both grains are shattered into small fragments (Jones et al. 1996). So one objective of this paper is to study the influence of radiative acceleration on the outcome and time scales of

grain coagulation and shattering, applying a more sophisticated radiation hydrodynamic code in contrast to former work in this field.

The size distribution of the dust grains influences the gas dynamical behavior of collapsing molecular clumps significantly. The loss of small grains via coagulation lowers the optical and ultraviolet extinction. This in turn affects the transport of radiation in the cloud, the radiative acceleration of the dusty gas (via hydrodynamic drag with the accelerated dust particles), and ultimately the final product.

We have carried out numerical simulations of the dust dynamics and grain growth in a collapsing protostellar cloud clump. The gas-dust mixture is treated as a hydrodynamical multi component fluid: each dust component is treated as a separate fluid which interacts with the gas component via hydrodynamic drag. The dust components interact with each other directly via coagulation, cratering and shattering and indirectly due to their effect on the gas and the radiation field. In this first investigation we assume compact spherical grains. This seems to be a reasonable assumption providing a first exploration of the problem and giving results that can be compared with more sophisticated dust models (fractal grains).

Continuum radiation transport from the radio to the FUV is done in a multi angle, multi frequency manner to include the effects of changes in the wavelength-dependent extinction of the dust. A detailed model of the microphysics of the coagulation and shattering process is applied together with a self-consistent calculation of the opacities from the size distribution of the grains (section 2). In section 3 we describe our code together with test calculations for the solver of the coagulation equation. Section 4 introduces our standard cloud model, which supplies the initial values for the simulations (section 5). In section 6 the results are discussed.

2. Microphysics of the grains

2.1. Dust dynamics and coagulation

We treat the dust grains as compact silicate spheres. The dust particles are coupled to the gas by dynamical friction. The Epstein coupling law (Epstein 1923; Weidenschilling 1977) is applied with its extension to superthermal velocities (Yorke & Krügel 1977). This is valid because the mean free path in the cloud clump is several orders of magnitude larger than typical grain radii. The grains are accelerated by the gravitational potential Φ of the cloud and by radiation pressure. Gyration about magnetic field lines is neglected. Thus, the total acceleration of dust component i with radius a_i , mass m_i , velocity \vec{v}_i and extinction coefficient for radiation pressure $\kappa_{\lambda,i}^p$ is:

$$\left(\frac{\partial \vec{v}_i}{\partial t}\right) = \left(\frac{\partial \vec{v}_i}{\partial t}\right)_{\text{grav}} + \left(\frac{\partial \vec{v}_i}{\partial t}\right)_{\text{rad}} + \left(\frac{\partial \vec{v}_i}{\partial t}\right)_{\text{ww}}$$

$$= -\nabla\Phi + \frac{1}{c} \int_0^\infty \kappa_{\lambda,i}^p \vec{F}_\lambda d\lambda \\ + \frac{4\pi}{3} \rho \frac{a_i^2}{m_i} \sqrt{c_s^2 + (\vec{v} - \vec{v}_i)^2} (\vec{v} - \vec{v}_i)$$

where \vec{F}_λ is the wavelength-dependent radiative flux, c the speed of light, ρ the gas density, \vec{v} its velocity and c_s the speed of sound. From this it appears obvious that grains of different sizes will gain systematic differing velocities in a collapsing cloud clump. In addition, the dust moves with random velocities caused by Brownian motion and turbulence. In the present calculations we neglect turbulence because of the dominance of differential radiation acceleration (see section 5). The random velocity between grain i and grain j becomes:

$$\langle v_{ij}^2 \rangle = \langle v_{ij}^2 \rangle_{\text{Brown}} = \frac{8kT}{\pi} \frac{m_i + m_j}{m_i m_j}$$

Brownian motion is only relevant for small particles ($< 1 \mu\text{m}$). For the bulk density of the silicates we took $\rho_{\text{bulk}} = 3 \text{ g cm}^{-3}$ with a sublimation temperature of 1500 K.

Once the relative velocities are known, the growth of the dust grains is described by the coagulation equation:

$$\left(\frac{\partial n(m)}{\partial t} \right)_{\text{coag}} = \frac{1}{2} \int \int \alpha(m', m'') n(m') n(m'') \\ \delta(m - m' - m'') dm' dm'' \\ - n(m) \int \alpha(m, m') n(m') dm'$$

with:

$$\alpha(m', m'') = p \pi (a(m') + a(m''))^2 |(\vec{v}(m') - \vec{v}(m''))|$$

Here $n(m)$, $a(m)$ and $\vec{v}(m)$ are the number density per unit mass interval, radius and velocity of grains with mass m , and δ is the Dirichlet delta function. Following Chokshi et al. (1993) the sticking probability p is considered perfect ($p = 1$) up to a critical velocity, above which p becomes zero. For material coefficients we assumed a thin ice layer on the silicate grains (an improved model is described in section 5.4). Without ice coatings two $0.1 \mu\text{m}$ silicate grains will stick up to a relative velocity of 10^2 cm s^{-1} , whereas the critical velocity for two ice-coated grains is more than an order of magnitude larger.

When two dust particles stick together, we assume they form another compact spherical grain with the sum of the colliding masses. This is a rough approximation, since laboratory experiments and numerical simulations show that coagulated clusters of dust grains can be rather fluffy (Blum & Münch 1993; Meakin & Donn 1988; Ossenkopf 1993). This has a number of important effects on the microphysics of the grain growth process. Because the gas-dust coupling depends on the specific cross section a_i^2/m_i , the fluffy coagulates are

better coupled to the gas than their compact counterparts, and their relative velocities will be correspondingly less. Furthermore, sticking can be more efficient due to the larger number of possible vibrational excitation modes in fractal coagulates which provide a wider channel to absorb the impacting projectile's kinetic energy (Poppe & Blum 1996; Wurm 1997).

2.2. Cratering and shattering

When the relative velocity between two grains rises above the critical sticking velocity, coagulation ceases and the grains bounce. At somewhat higher velocities ($> 2.7 \text{ km s}^{-1}$ for silicates) cratering occurs, and when the collision velocity is large enough, the grains will be shattered into small fragments. Jones et al. (1996) performed detailed calculations of the ejected mass and the size distribution of the fragments. We use their results in considering the shattering contribution:

$$\left(\frac{\partial n(m)}{\partial t} \right)_{\text{shat}} = \frac{1}{2} \int \int \beta(m', m'') n(m') n(m'') \\ \gamma(m, m', m'', |\vec{v}(m') - \vec{v}(m'')|) dm' dm'' \\ - n(m) \int \beta(m, m') n(m') dm'$$

with:

$$\beta(m', m'') = q \pi (a(m') + a(m''))^2 |(\vec{v}(m') - \vec{v}(m''))|$$

The shattering probability q determines the onset of the erosive processes, whereas the function γ describes the redistribution of the ejected or shattered mass. In order to calculate γ the equations and material coefficients for silicate given by Jones et al. (1996) are used. The size distribution exponent of the shattered fragments is set to -3.5 . We assume an instant assimilation of the debris particles ($\approx 0.01 \mu\text{m}$) in the low-mass bins. This approximation is valid as long as the correlation time scale τ_i is smaller than the numerical time step:

$$\tau_i = \frac{\Delta v_i}{\left(\frac{\partial v_i}{\partial t} \right)_{\text{ww}}} = \frac{\rho_{\text{bulk}} a_i}{c_s \rho} \approx 10^{-18} \rho^{-1} [\text{yr}]$$

A typical numerical time step is about one year, which is larger than τ_i as long as $\rho \gtrsim 10^{-18} \text{ g cm}^{-3}$ (true for regions where shattering is important). Our numerical treatment of coagulation and shattering is briefly sketched in the appendix.

2.3. Opacities

The specific extinction coefficients and radiation pressure cross sections were calculated by Mie theory using the optical constants for “astronomical” silicate of Draine & Lee (1984) constructed from observational data of the diffuse interstellar medium. The total specific extinction then reads:

$$\kappa_{\lambda,i}^{\text{ext}} = Q_{\lambda,i}^{\text{ext}} \frac{\pi a_i^2}{m_i}$$

$$\kappa_{\lambda}^{ext} = \frac{\sum_{i=1}^N \rho_i \kappa_{\lambda,i}^{ext}}{\sum_{i=1}^N \rho_i}$$

$$\kappa_{\lambda,i}^p = \kappa_{\lambda,i}^{ext} (1 - A_{\lambda,i} g_{\lambda,i})$$

Here $Q_{\lambda,i}^{ext}$ is the dimensionless efficiency factor for extinction of grain i , $A_{\lambda,i}$ the albedo and $g_{\lambda,i} = (\cos \theta)_{\lambda,i}$ the asymmetry parameter, all of which are calculated by Mie theory using the complex dielectric function. Figure 1 shows the specific extinction of MRN dust consisting of grains with radii from 5 nm to 5 μm . It is given in cross section per gas mass (dust-gas mass ratio is 0.01).

To show the contributions of the different grain sizes to the total extinction, opacities for particle radii of 5 nm, 0.1 μm and 5 μm are displayed in figure 1 (each normalized to a dust-gas mass ratio of 0.01). The characteristic 10 μm silicate feature is caused by sub- μm dust particles. The visual and ultraviolet extinction is dominated by the contribution of small (sub- μm) grains. The grain radii used in the numerical simulations are given in table 1.

3. The Numerical Model

3.1. Method

To simulate the evolution of a collapsing molecular cloud clump we apply an implicit multi component 1D radiation hydrodynamic code in spherical symmetry. The equations of hydrodynamics are solved together with the Poisson equation for self-gravity and the angle-dependent, frequency-dependent equations of radiation transport (Yorke 1979, 1980):

$$\mu \frac{\partial I_{\lambda}}{\partial r} + \frac{1 - \mu^2}{r} \frac{\partial I_{\lambda}}{\partial \mu} = -I_{\lambda} \sum_{i=1}^N (1 - A_{\lambda,i}) \kappa_{\lambda,i}^{ext} \rho_i + j_{\lambda}$$

$$- \sum_{i=1}^N A_{\lambda,i} \kappa_{\lambda,i}^{ext} \rho_i \left[I_{\lambda} - \frac{1}{2} \int_{-1}^1 I_{\lambda}(\mu') \Theta_{\lambda}(\mu, \mu') d\mu' \right]$$

where $I_{\lambda} = I_{\lambda}(r, \mu)$ is the intensity of radiation of wavelength λ at radius r in the direction $\mu = \cos \theta$, j_{λ} is the emissivity and Θ the scattering phase function.

Table 1: Radii of the calculated dust species.

| # | a [μm] | # | a [μm] | # | a [μm] |
|---|------------------------|----|------------------------|----|------------------------|
| 1 | 0.005 | 8 | 0.064 | 15 | 0.829 |
| 2 | 0.007 | 9 | 0.093 | 16 | 1.195 |
| 3 | 0.010 | 10 | 0.134 | 17 | 1.721 |
| 4 | 0.015 | 11 | 0.193 | 18 | 2.480 |
| 5 | 0.022 | 12 | 0.277 | 19 | 3.573 |
| 6 | 0.031 | 13 | 0.400 | 20 | 5.147 |
| 7 | 0.045 | 14 | 0.576 | | |

The frictional coupling of dust and gas is approximated by the asymptotic limit (no time dependence in the interaction term). Where the temperature T_i of grain component i exceeds its sublimation temperature, the grains are removed from the flow. Where conditions allow, dust grains are allowed to flow back into dust-free regions with their calculated velocity, i.e., dust does not spontaneously reform when the calculated temperature drops.

The coagulation equation is computed between hydrodynamic time steps. The coagulation substep is also performed by an implicit solver which strictly conserves mass. The dust distribution function is binned into 20 logarithmically spaced mass intervals. Initially, we start with an MRN size distribution — the number density per unit radius scales as:

$$n(a) \propto a^{-3.5}$$

This transforms to a bin mass distribution

$$m(m) dm \propto m^{-5/6} dm \propto m^{1/6} d \ln m$$

The dashed curve in Figure 11 shows this assumed initial mass distribution. Whenever the coagulation equation is solved, the revised dust densities are used to update the opacities in each radial cell. Therefore, every change in the size distribution has direct dynamical consequences for the further evolution.

The numerical grid consists of about 100 to 200 logarithmically spaced radial cells covering the protostellar envelope from $3 \cdot 10^{13}$ cm to $\approx 10^{17}$ cm. Frequency-dependent radiation transport is done at 64 different wavelengths ranging from 0.1 μm to 0.5 cm. For the numerical method discussed by Yorke (1979, 1980) the number of directions included in the radiation transfer varies from 103 to 203 in the outermost zone (equal to the number of radial cells + 3) to 4 at the center. At the inner border of the mesh the infalling material is accumulated into a central object; its mass M_* — together with the mass accretion rate \dot{M}_* — determines the core luminosity according to the formula:

$$L_* = L_{\odot} \left(\frac{M_*}{M_{\odot}} \right)^3 + \frac{6}{7} \frac{GM_* \dot{M}_*}{R_*}$$

For the numerical results discussed here the radius R_* of the central hydrostatic core has been set to the constant value $5 R_{\odot}$. The main contribution to the stellar luminosity results from the accretion shock (more than 99% in early phases). At the outermost radius mass is allowed to flow out freely, but no mass is allowed to enter into the computational grid (semipermeable outer boundary).

3.2. Testing the code

We tested the coagulation solver by comparing with analytical solutions (Wetherill 1990). These exist for simple kernels in the integrals of the coagulation equation, e.g.:

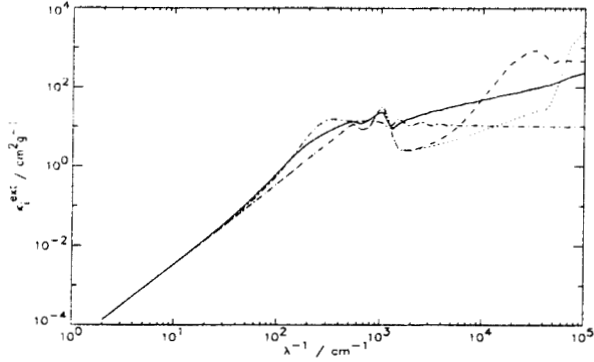


Fig. 1.— Specific extinction coefficients of dusty gas (“astronomical silicates”) with all grains having a radius of $a = 5$ nm (dotted line), $a = 0.1 \mu\text{m}$ (dashed line) and $a = 5 \mu\text{m}$ (dot-dashed line). The solid line shows the specific extinction for a MRN distribution of all grain sizes.

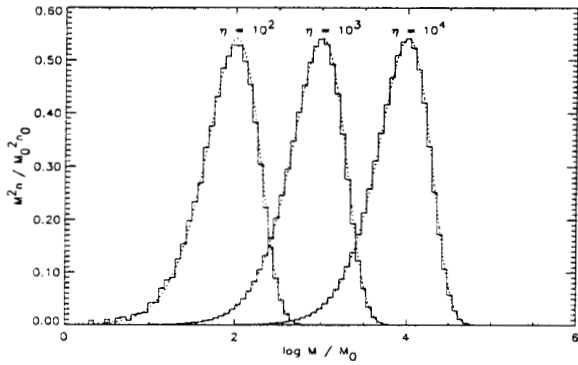


Fig. 2.— Comparison of our computed solutions of the coagulation equation (solid lines) with the exact solutions (dotted). The distributions of grain masses are shown at dynamical time scales $\eta = 10^2, 10^3$ and 10^4 respectively (see Wetherill 1990).

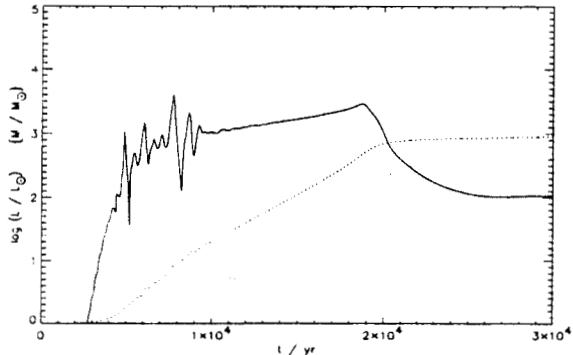


Fig. 3.— Time evolution of the core luminosity (solid line) and the core mass (dotted line) of model C_3MS. About 6 free-fall times are displayed.

$$\begin{aligned}\alpha_0 &= 1 \quad \text{cm}^3 \text{s}^{-1} \\ \alpha_1 &= (m_i + m_j) \quad \text{g}^{-1} \text{cm}^3 \text{s}^{-1} \\ \alpha_2 &= m_i m_j \quad \text{g}^{-2} \text{cm}^3 \text{s}^{-1}\end{aligned}$$

We calculated the solution for the constant kernel (i.e., $\alpha = \alpha_0$) with our solver (see Figure 2), starting with all n_0 grains in the bin with the lowest mass and evolving several dynamical time scales $\eta = \alpha n_0 t$. With our choice of binning resolution we can well reproduce the exact solution. At lower binning resolutions we are still able to represent the location of the maximum. However, the width of the distribution and its value at maximum suffered when significantly fewer bins were employed. Total dust mass was always conserved within rounding errors. For the shattering scheme (which is by definition mass conserving) we used the same coagulation solver with appropriate integral kernels (see appendix). Thus, we can rely on the tested mass conservation and convergence of this solver.

4. The protostellar cloud model

The initial condition for our calculations is a spherically symmetric, centrally condensed ($\rho \propto r^{-1}$ with a cut off close to $r = 0$), isothermal ($T = 20$ K), non-rotating molecular cloud clump. We assume an initial dust size distribution according to a power law with an exponent -3.5 for grain radii between 5 nm and $5 \mu\text{m}$ (see dotted curve in figure 11). The dust’s mass contribution is set to 0.01 ; all velocities are initially zero. The clump extends out to $2 \cdot 10^{16}$ cm, where the density falls off rapidly ($\propto r^{-8}$). Selected parameters are given in table 2. All calculations are conducted over several free-fall time scales t_{ff} , until most of the mass either accumulates in the center or escapes through the outermost radius.

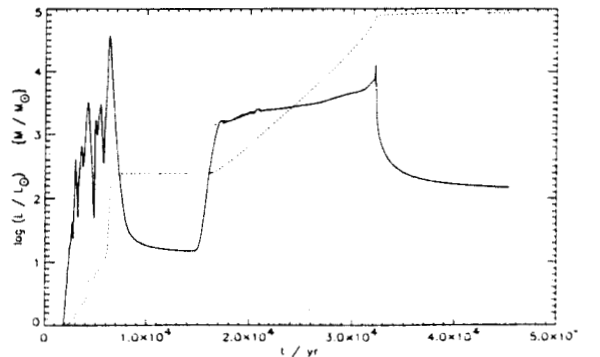


Fig. 4.— Time evolution of the core luminosity (solid line) and the core mass (dotted line) of model C_5MS. The corresponding free-fall time is $t_{\text{ff}} = 3.9 \cdot 10^3$ yr. A strong luminosity peak at 6000 yr essentially stops the mass accretion onto the core for about 10000 yr.

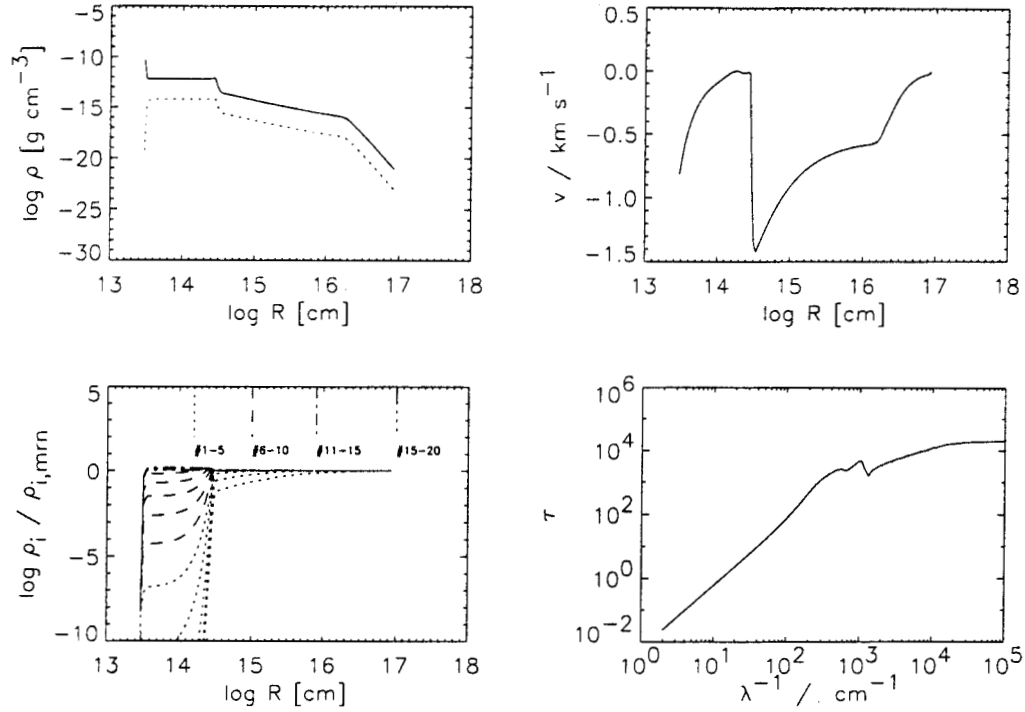


Fig. 5.— Model C.3MS at 2270 yr. Displayed are: densities of gas (solid line) and total dust (dotted line; u.l.), velocity of gas (u.r.), depletion of the dust grains (l.l.), total optical depth through the envelope (l.r.). In the depletion diagram the dust is plotted in groups of five components for display purposes.

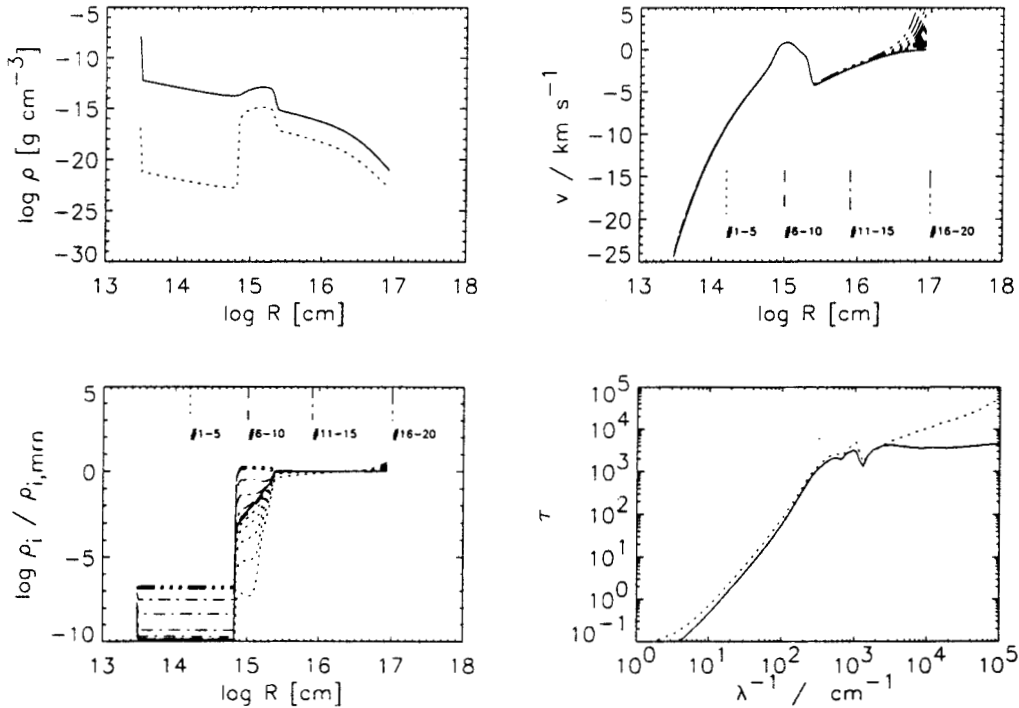


Fig. 6.— Model C.3MS at 7068 yr. Symbols and lines have the same meanings as in figure 5, except for the u.r. frame, where velocities of both gas and dust components are shown. For the velocity and depletion diagrams the dust is plotted in groups of five components for display purposes. The optical depth through the cloud without coagulation is also shown as dotted line (l.r.).

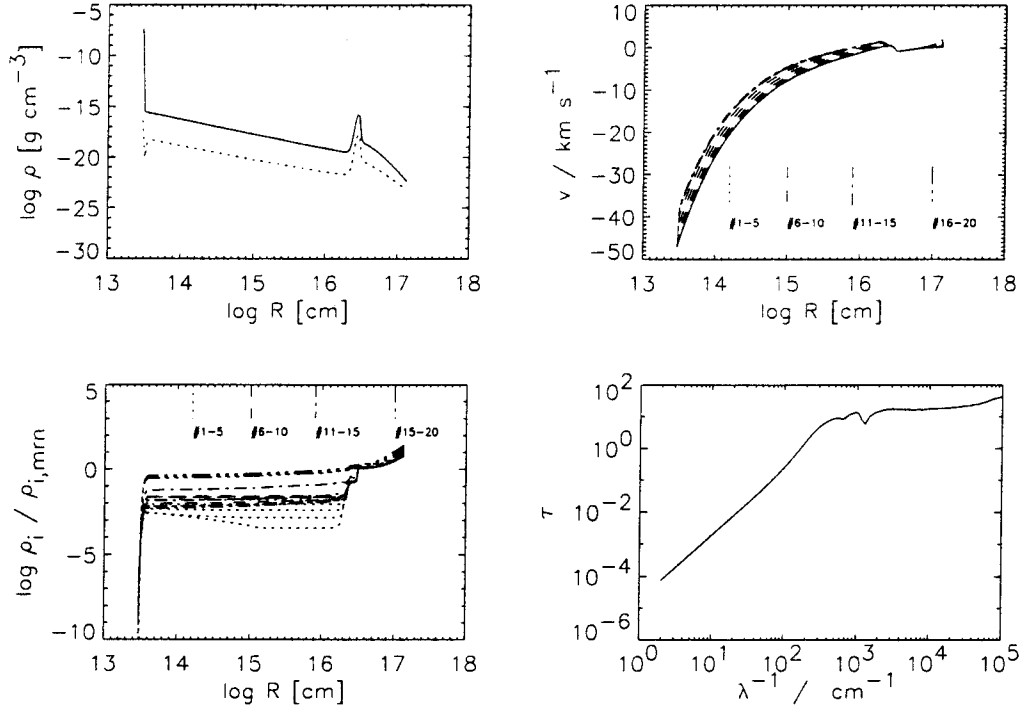


Fig. 7.— Model C.5MS at 10800 yr. Symbols and lines have the same meanings as in figures 5 and 6.

Table 2: Characteristics of the cases considered. M_{tot} = beginning clump mass; t_{ff} = initial free-fall time scale; t_{evol} = total evolutionary time calculated; M_* = final mass of central core. Models denoted by “C-” include the effects of coagulation.

| model | M_{tot} [M_{\odot}] | t_{ff} [10^4 yr] | t_{evol} [10^4 yr] | M_* [M_{\odot}] |
|------------|-------------------------------------|---------------------------------|-----------------------------------|--------------------------|
| 3MS | 3.0 | 0.50 | 5.8 | 3.0 |
| C.3MS | 3.0 | 0.50 | 3.2 | 3.0 |
| 5MS | 5.0 | 0.39 | 4.8 | 4.4 |
| C.5MS | 5.0 | 0.39 | 4.5 | 4.9 |
| 8MS | 8.0 | 0.31 | 5.6 | 6.8 |
| C.8MS | 8.0 | 0.31 | 6.1 | 7.8 |
| 10MS | 10.0 | 0.27 | 5.5 | 6.6 |
| C.10MS | 10.0 | 0.27 | 6.8 | 6.5 |
| C.10MS.i | 10.0 | 0.27 | 6.7 | 7.2 |
| C.10MS.i10 | 10.0 | 0.27 | 6.7 | 7.4 |

5. Results

The evolution of all models is influenced strongly by the luminosity of the central object. During the initial phases of high mass accretion, the resulting accretion shock luminosity inhibits infall by radiatively accelerating the dust, well coupled to the gas. Thus, the accretion rate and the associated luminosity diminish until — after several oscillations — a quasi-steady state is established. Table 2 shows the final core masses resulting from each simulation conducted. For the $3 M_{\odot}$ case all mass accumulates in the center. Starting from about five solar masses, significant differences are found between calculations which include dust coagulation and those with a fixed grain size spectrum.

5.1. Model C.3MS

Figure 3 shows the time evolution of core luminosity and core mass for model C.3MS. The early phase of strong variability is followed by a rather smooth and steady accretion, until all the mass has accumulated in the core. The variable phase lasts approximately one free-fall time.

Figure 5 displays selected physical variables at an early stage of the collapse, $t = 2270$ yr. An accretion shock has developed at $\log r = 14.5$. Due to the high gas densities and low core luminosity, gas and dust are still well coupled. The depletion¹ of the different dust components (lower left frame of Fig. 5) shows that

¹ Here, “depletion” is defined as the reduction of mass in a given bin with respect to the initial MRN-distribution.

inside the shock front all the small grains have been removed by coagulation. Groups #1–5 (5 nm – 20 nm) and #6–10 (30 nm – 0.1 μm) are highly depleted. This is reflected in the total optical depth. In particular, the visual and ultraviolet contributions are lowered due to the loss of small grains.

When the core luminosity rises to several thousand L_{\odot} , the mass inside the accretion shock is accelerated outward and a shell of dusty material expands. At the same time, coagulation continues to remove small dust grains from the envelope. Figure 6 shows the envelope structure at 7068 yr. Again, the ongoing coagulation manifests itself in the modified total optical depth at visual and ultraviolet wavelengths. At the density maximum at $\log r = 15.2$ the mean size distribution exponent is -2.7 ; over the entire volume it is -3.2 . Inside $\log r = 14.8$ the dust has been destroyed due to the high grain temperatures there. At the outer edge of the cloud the dust grains achieve relative velocities of several km s^{-1} .

For purposes of comparison, the wavelength-dependent optical depth through the envelope is displayed in figure 6 for calculations both with and without coagulation. At a wavelength of 0.1 μm the optical depth is lowered by one order of magnitude when coagulation is included in the calculations. This emphasizes the important feedback of a modified dust size spectrum on the dynamics. Although UV-radiation will be processed quickly into the IR close to the accretion shock, it is this region which determines the dynamics and the mass flow onto the stellar core. Although an observer outside the core will not be able to detect any radiation from this wavelength regime, it's not irrelevant for the structure of the flow. For luminous central cores, coagulated dust is supposed to enable the gas to flow toward the center more easily (Wolfire & Cassinelli 1987). We do see a trend in this direction, but the differences are not overwhelming. Further increasing the central core's luminosity will lead to high relative velocities and consequently to dust shattering, as discussed in the following section.

5.2. Model C_5MS

When the cloud mass is increased to 5 M_{\odot} , higher accretion luminosities are attained. The initial evolution is similar to the 3 M_{\odot} model. In later phases relative velocities of several km s^{-1} between the different grains could lead to significant destruction of μm -size dust particles. In figure 7 model C_5MS is shown at 10800 yr. The corresponding evolution of core luminosity and core mass is plotted in figure 4.

At this stage of evolution a density maximum has developed at $\log r = 16.5$. This feature is caused by a peak in the core luminosity at 6000 yr. Radiation accelerates dusty protostellar material away from the star. This material piles up in a thin shell of dust and gas (e.g., Yorke 1979). Inside the shell the gas flows toward the center and the dust particles have relative veloci-

ties of several km s^{-1} . Figure 9 shows the velocities of selected dust components.

Relative velocities of about 5 km s^{-1} are achieved between nm-sized and μm -sized particles. At $\log r = 14$ ($T_{\text{gas}} \approx 200$ K) Brownian motion leads to a relative velocity $v_{\text{rel}} = 0.004 \text{ km s}^{-1}$ and turbulence ($\alpha = 0.01$) would lead to $v_{\text{rel}} = 0.01 \text{ km s}^{-1}$. This demonstrates the dominance of differential radiative acceleration, at least for intermediate-mass stars, and the need to include destructive processes in future simulations. In the overall mass spectrum most of the mass resides in μm -sized grains. Shattering is not sufficiently effective to transfer mass back to nm-sized particles. One should keep in mind that most mass is located in the dense shell in outer zones of the integration domain, which dominates the total mass spectrum. So dust shattering at radii close to the central stellar core will not be seen in the overall mass distribution but may well determine the local dynamics due to opacity variations.

When sticking parameters for a pure quartz surface of the grains are used in the simulations (in contrast to an icy surface), coagulation is less effective due to the lowered critical sticking velocity (figure 8). The maximum depletion outside of $\log r = 15$ is $\approx 10^{-3.5}$. At smaller distances from the star the effects of grain bouncing and grain shattering enhances the abundance of the smallest grains to $10^{-2.5}$. During the subsequent evolution material from the dense shell can flow toward the star in a quasi-steady state (figure 4) until again nearly all mass has accumulated in the center.

5.3. Model C_10MS

In the 10 M_{\odot} simulation (model C_10MS) the effects of bouncing and shattering are more important. Here, coagulation is not able to lower the ultraviolet extinction significantly (cf. figure 10). The maximum in the mass spectrum at $m/m_0 = 10$ (shown for $t = 4300$ yr in figure 11) represents shattered fragments. At this stage relative velocities of about 10 km s^{-1} initiate a drastic enhancement of nm-sized dust particles. The overall dust size distribution in the clump becomes steeper.

It seems that shattering can destroy all the work coagulation has done in the cloud core prior to collapse. For this reason we also investigated the influence of the sticking strength on the coagulation process for the 10 M_{\odot} case.

5.4. Models C_10MS_i and C_10MS_i10

As shown in figure 8, the assumed structure of the grain surface influences the outcome of a coagulation calculation significantly. For purposes of comparison we altered our treatment of dust interior to the ice sublimation radius. Within the ice sublimation zone $T_{\text{ice}} > 125$ K, sticking coefficients for silicate surfaces were taken; otherwise we use the ice sticking coefficients (model C_10MS_i). We also have conducted a simulation (model C_10MS_i10) with the sticking energies larger by a factor of 100 (critical sticking velocities

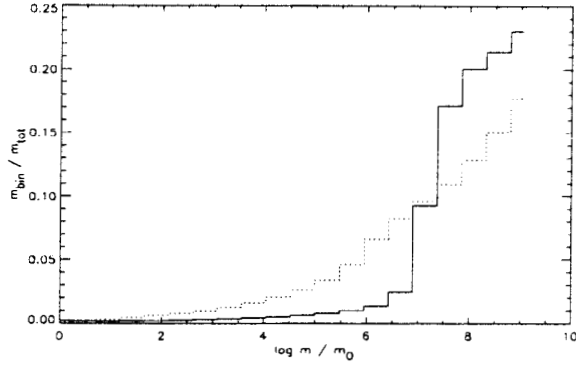


Fig. 8.— Dust mass distribution of model C.5MS at 10800 yr (solid line, icy grain surfaces). The corresponding size distribution exponent is -3.2 . For comparison, the resulting mass distribution assuming quartz surface parameters (dotted line).

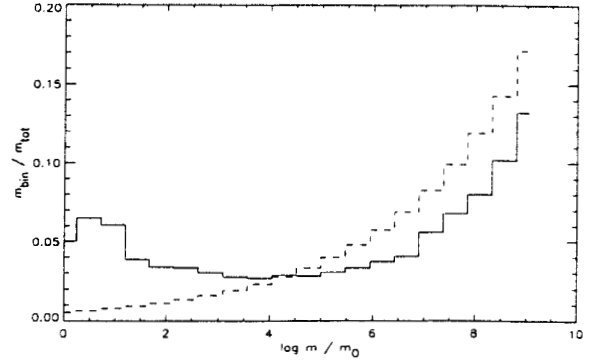


Fig. 11.— Dust mass distribution of model C.10MS at 4300 yr. The corresponding size distribution exponent is -3.9 . For comparison the assumed initial MRN mass distribution (exponent -3.5) is shown as a dashed line.

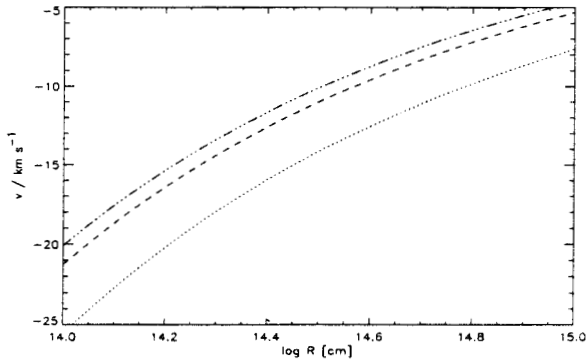


Fig. 9.— Velocities of dust #1 (dotted), #10 (dashed) and #20 (dot-dashed, see table 1). An enlargement of the upper right panel of figure 7 is displayed.

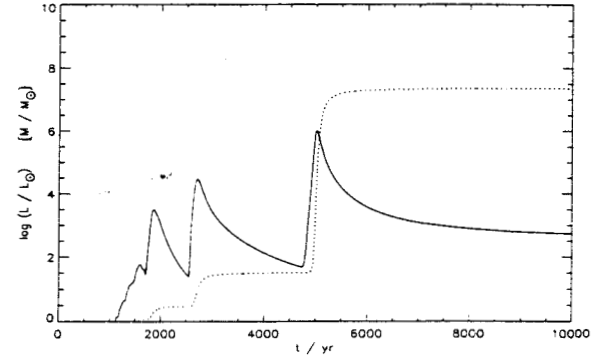


Fig. 12.— Time evolution of the core luminosity (solid line) and the core mass (dotted line) of model C.10MS.i10. The corresponding free-fall time is $t_{ff} = 2.7 \cdot 10^3$ yr.

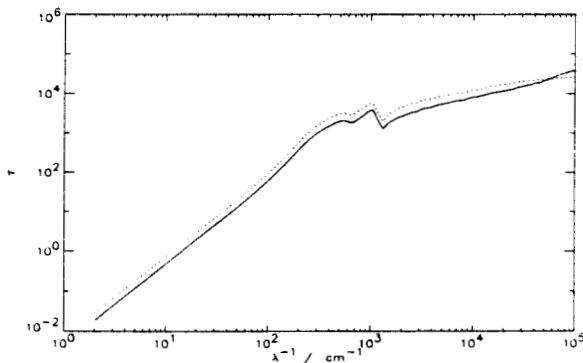


Fig. 10.— Optical depth through the cloud without (solid line; model 10MS) and with coagulation and shattering (dotted line; model C.10MS) at an equivalent stage of evolution.

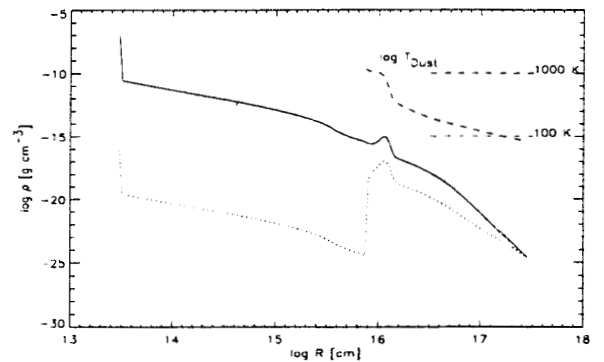


Fig. 13.— Model C.10MS.i10 at 5100 yr: Density of gas (solid line), density of total dust (dotted line) and dust temperature (dashed line; u.r. corner). The ice sublimation radius is at $8 \cdot 10^{16}$ cm.

increase by a factor of 10) to be compatible with experimental results (Poppe & Blum 1996; Bridges et al. 1996; Supulver et al. 1997). Figures 12, 13, and 14 show the time dependence of the core luminosity and core mass, the resulting density distribution of gas and dust, and the dust temperature and overall mass spectrum, respectively.

The reduced sticking strength inside the ice sublimation radius hinders effective coagulation of the debris particles (compare to figure 11 where ice coefficients were taken throughout). Nevertheless, the mass of the resulting central core is *increased* by about 10% in comparison to model C.10MS. We note, however, that mass accretion onto the central core is rather rapid and variable for the $10 M_{\odot}$ cases. The immediate vicinity of dust sublimation acts as a sensitive valve which allows mass infall at high stellar luminosities and thus determines the final central mass. It is important to treat this region with utmost care when modeling high mass star formation.

6. Conclusions

We have found dust coagulation to be an important process during the collapse of a molecular cloud core. Time scales as short as 10^3 yr (i.e., shorter than typical free-fall time scales) are sufficient for coagulation to modify the dust size distribution. Brownian motion and differential radiative acceleration remove the small grains from the size spectrum and convert them into μm -sized particles. The visual and ultraviolet extinction is reduced by these changes in the grain size spectrum.

Relative velocities of several km s^{-1} are possible. Thus, effects of bouncing and shattering of dust particles should also be taken into account in collapse simulations. Particle sputtering is not important in this early phase of protostellar evolution, assuming typical threshold velocities between gas and dust of ≈ 50

km s^{-1} (Wolfire & Cassinelli 1987; Jones et al. 1996). Higher clump masses ($>10 M_{\odot}$) could conceivably imply a more effective shattering of the μm -sized grains and thus an enhancement of the specific dust extinction. This hypothesis remains to be demonstrated, however; it will require a careful analysis of the interactions of radiation and matter in accreting accretion disks in an environment where radiation, coagulation, and/or shattering dominate the dust evolution.

In contrast to the investigation of Weidenschilling & Ruzmaikina (1994), we simulated the collapse of a protostellar cloud clump by numerical radiation hydrodynamic calculations. Thus, we were able to follow the evolution of the grains through the entire accretion flow where dust is present — i.e., through an outer accretion shock, within the dense circumstellar dust shell which often forms, down to the radius of sublimation of the grains. We found that, for a luminous central radiation source, differential radiative acceleration is able to supersede turbulence as the main contributor to relative velocities between dust grains during the collapse phase.

An enhancement of the sticking energies to fit the results of recent experiments does not increase the final central mass significantly in comparison to conservative assumptions about grain sticking. It also cannot completely prevent dust cratering and shattering during the formation of intermediate-mass stars.

We have not investigated the further evolution of the μm -sized grains, nor have we considered modifications of the internal structure of the particles. Because coagulated grains are presumably fractal, the dust-gas interactions and the net optical properties can deviate from the “solid grain” characteristics we have assumed here. For more fluffy coagulates the relative velocities will be reduced due to an enhanced coupling to the gas component. On the other hand, fractal grains could shatter easily because their binding energy is very low (Dominik & Tielens 1997). This makes it hard to decide what the differences to simple bulk grains will be without further numerical simulations. These effects are to be addressed in greater detail in a subsequent paper. The dust evolution during the formation of a protostellar accretion disk poses another important problem. Results of 2D radiation hydrodynamic simulations of rotating and collapsing molecular cloud clumps currently being prepared for publication indicate that indeed dust reprocessing begins at a very early stage of contraction and collapse (Suttner et al. 1999).

Acknowledgments: We thank Peter Bodenheimer, Thomas Henning and Rainer Schröpler for helpful discussions. The research described in this paper was carried out by the Jet Propulsion Laboratory (JPL), California Institute of Technology, and was sponsored by the “Deutsche Forschungsgemeinschaft” (DFG) and the National Aeronautics and Space Administration (NASA). We are grateful to DFG for financial support under the “Physics of Star Formation” program

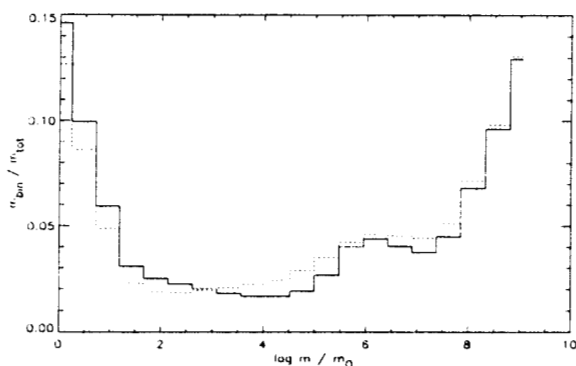


Fig. 14.— Dust mass distribution of model C.10MS_i10 with our modified dust model at 5100 yr (solid line). The dotted line denotes the mass spectrum resulting from the lower (i.e., Chokshi et al.) sticking coefficients (model C.10MS_i).

and to NASA for their support of the authors' research at JPL and for their support through a special NASA astrophysics theory program which funds a joint Center for Star Formation Studies at NASA/Ames Research Center, UC Berkeley, and UC Santa Cruz. The calculations were performed on computers operated by the "Rechenzentrum der Universität Würzburg", the JPL/Caltech Supercomputing Project, and the "Hochleistungsrechenzentrum" in Jülich.

Appendix

Here the numerical solution scheme of the combined coagulation/shattering equation is described. To solve this nonlinear differential equation the integral is written as a sum over the N discrete mass bins:

$$\left(\frac{\partial n_k}{\partial t}\right)_{\text{coag/shat}} = \frac{1}{2} \sum_{i=1}^N \sum_{j=1}^N (\alpha_{ij} d_{ijk} + \beta_{ij} g_{ijk}) n_i n_j - n_k \sum_{i=1}^N (\alpha_{ij} + \beta_{ij}) n_i$$

with:

$$d_{ijk} = \begin{cases} \frac{m_i + m_j}{m_k} & \text{if } m_i + m_j \in [m_k - \frac{\Delta m_k}{2}, m_k + \frac{\Delta m_k}{2}] \\ 0 & \text{else} \end{cases}$$

$$g_{ijk} = \frac{m_i + m_j}{m_k} G_k(m_i, m_j, \delta v_{ij}),$$

$$G_k(m_i, m_j, \delta v_{ij}) \in [0, 1], \quad \sum_{k=1}^N G_k(m_i, m_j, \delta v_{ij}) = 1$$

The mass bins are spaced logarithmically with median mass m_k and width Δm_k . The variable n_k is the particle density of dust grains with mass m_k per unit mass interval. The shattered particles are distributed according to the model of Jones et al. (1996). This is controlled by the discrete distribution function $G_k(m_i, m_j, \delta v_{ij})$. The numerical scheme strictly conserves mass. Finally the equation is discretized using backward time differences:

$$\left(\frac{n_k^* - n_k}{\Delta t}\right)_{\text{coag/shat}} = \frac{1}{2} \sum_{i=1}^N \sum_{j=1}^N (\alpha_{ij} d_{ijk} + \beta_{ij} g_{ijk}) n_i^* n_j^* - n_k^* \sum_{i=1}^N (\alpha_{ij} + \beta_{ij}) n_i^*$$

This system of equations can be solved by inverting a nonlinear $N \times N$ matrix, which we do for each cell of the 1D grid using a multidimensional Newton iteration scheme.

REFERENCES

Blum, J., Münch, M., 1993, *Icarus*, 106, 151

- Blum, J., Wurm, G., Kempf, S., Henning, Th., 1996, *Icarus*, 124, 441
- Bridges, F.G., Supulver, K.D., Lin, D.N.C., Knight, R., Zafra, M., 1996, *Icarus*, 123, 422
- Chokshi, A., Tielens, A.G.G.M., Hollenbach, D., 1993, *ApJ*, 407, 806
- Dominik, C., Tielens, A.G.G.M., 1997, *ApJ*, 480, 647
- Draine, B.T., Lee, H.M., 1984, *ApJ*, 285, 89
- Epstein, P., 1923, *Phys. Rev.*, 22, 710
- Fischer, O., Henning, Th., Yorke, H.W., 1994, *A&A*, 284, 187
- Jones, A.P., Tielens, A.G.G.M., Hollenbach, D., 1996, *ApJ*, 469, 740
- Kahn, F.D., 1974, *A&A*, 37, 149
- Mathis, J.S., Rumpl, W., Nordsieck, K.H., 1977 (MRN), *ApJ*, 217, 425
- Meakin, P., Donn, B., 1988, *ApJ*, 329, L39
- Mizuno, H., Markiewicz, W.J., Völk, H.J., 1988, *A&A*, 195, 183
- Nakagawa, Y., Nakazawa, K., Hayashi, C., 1981, *Icarus*, 45, 517
- Ossenkopf, V., 1993, *A&A*, 280, 617
- Poppe, T., Blum, J., 1996, *Adv. Space. Res.*, 20, 1595
- Schmitt, W., Henning, Th., Mucha, R., 1997, *A&A*, 325, 569
- Suttner, G., Yorke, H.W., 1999, *ApJ*, in preparation
- Supulver, K.D., Bridges, F.G., Tiscareno, S., Lievore, J., 1997, *Icarus*, 129, 539
- Vrba, F.J., Coyne, G.V., Tapia, S., 1993, *AJ*, 105, 1010
- Weidenschilling, S.J., 1980, *Icarus*, 44, 172
- Weidenschilling, S.J., Ruzmaikina, T.V., 1994, *ApJ*, 430, 713
- Wetherill, G.W., 1990, *Icarus*, 88, 336
- Wolfire, M.G., Cassinelli, J.P., 1987, *ApJ*, 319, 850
- Wurm, G., 1997, PhD, Universität Jena
- Yorke, H.W., 1979, *A&A*, 80, 308
- Yorke, H.W., 1980, *A&A*, 86, 286
- Yorke, H.W., Henning T., 1994, in *Molecules in the Stellar Environment*, ed. U.G. Jørgensen, IAU Coll. 146, 186
- Yorke, H.W., Krügel, E., 1977, *A&A*, 54, 183